RESEARCH ARTICLE

Transport evidence of 3D topological nodal-line semimetal phase in ZrSiS

Junran Zhang[1], Ming Gao[1], Jinglei Zhang[2], Xuefeng Wang[1,†], Xiaoqian Zhang[1],
Minhao Zhang[1], Wei Niu[1], Rong Zhang[1], Yongbing Xu[1,3,‡]

[1] *National Laboratory of Solid State Microstructures, Collaborative Innovation Center of Advanced Microstructures,*
School of Electronic Science and Engineering, Nanjing University, Nanjing 210093, China
[2] *High Magnetic Field Laboratory of Chinese Academy of Sciences, Hefei 230031, China*
[3] *York-Nanjing Joint Centre (YNJC) for Spintronics and Nano Engineering, Department of Electronics,*
University of York, YO10 3DD, United Kingdom
Corresponding authors. E-mail: †xfwang@nju.edu.cn, ‡ybxu@nju.edu.cn

Topological nodal-line semimetal is a new emerging material, which is viewed as a three-dimensional (3D) analog of graphene with the conduction and valence bands crossing at Dirac nodes, resulting in a range of exotic transport properties. Herein, we report on the direct quantum transport evidence of the 3D topological nodal-line semimetal phase of ZrSiS with angular-dependent magnetoresistance (MR) and the combined de Hass-van Alphen (dHvA) and Shubnikov-de Hass (SdH) oscillations. Through fitting by a two-band model, the MR results demonstrate high topological nodal-line fermion densities of approximately 6×10^{21} cm^{-3} and a perfect electron/hole compensation ratio of 0.94, which is consistent with the semi-classical expression fitting of Hall conductance G_{xy} and the theoretical calculation. Both the SdH and dHvA oscillations provide clear evidence of 3D topological nodal-line semimetal characteristic.

1 Introduction

Three-dimensional (3D) topological semimetal phases represent new quantum states of matter, often viewed as a "3D graphene", and have attracted intensive studies in recent years [1–3]. The new emerging concepts including topological Dirac semimetals, topological Weyl semimetals, and topological nodal-line semimetals are different kinds of topological semimetals established experimentally so far. These materials exhibit novel quantum coherent transport behaviors for potential device applications with high bulk carrier mobility and large magnetoresistance (MR) [4–9]. Further, 3D topological Dirac semimetals such as Cd_3As_2 and Na_3Bi feature a linear dispersion four-fold degenerate band crossing at Dirac nodes occurring at discrete momentum points, which drives the modulated electronic accumulation in the lowest Landau level (LL) and results in the dominance of linear MR in high magnetic fields [5, 6, 10–12]. Weyl charges with opposite chirality can be observed in topological Weyl semimetals, which can simu-

late the chiral anomaly of quasiparticle transport proposed in high-energy physics. Such topological Weyl states have been demonstrated in many materials, including (Ta/Nb)(As/P) [13, 14], (Mo/W)Te$_2$ [4, 15–17]. Among them, perfectly compensated electron/hole pockets have been observed at the Fermi level of WTe$_2$, resulting in the classic MR resonance and an unsaturated MR up to the high magnetic field of 60 T [4]. In WTe$_2$, intriguing linear MR appears when the magnetic field is aligned both in the perpendicular and parallel directions [17]. When a large MR is suppressed by pressure, superconductivity arises owing to the possible Fermi level nesting [15]. Similar physics generating a large quadratic MR of up to 10 000 times has been observed at 9 T in TaAs [14]. PbTaSe$_2$ [1], PtSn$_4$ [2], and ZrSiS [18, 19] have been experimentally established for topological nodal-line semimetal, where Dirac bands cross along a one-dimensional line or a loop in momentum space, contrasted with Dirac band crossing at discrete momentum points in topological Dirac or Weyl semimetals.

Among the reported topological semimetals, ZrSiS has been observed to have other distinct properties. The

tetragonal structure of ZrSiS is formed from a stack of S-Zr-Si-Zr-S sandwich layers [3, 20]. Angle-resolved photoemission spectroscopy (ARPES) studies have revealed two types of Dirac cones in ZrSiS and ZrSiTe: one of them forms a closed nodal-line loop near the Fermi level and the other represents the first example of the theoretically-predicted Dirac cone state protected by non-symmorphic symmetry [3, 21]. Multiple Fermi surface pockets, such as diamond-shaped Fermi surface, have been demonstrated in ARPES studies [3, 18, 22]. In terms of the transport properties of ZrSiS, an extremely large, non-saturating MR and large anisotropy with different field directions have been observed [9, 22, 23]. Quasi-2D Dirac Fermi surfaces and a topological phase transition from nontrivial to trivial with altering angles have been observed [24]. Except for the traditional electrical/magnetic transport measurements, some novel methods have been performed on topological nodal-line semimetal ZrSiS and its series. For example, Dirac bands and Fermi surface enclosing the Dirac nodal-line with 3D character were revealed by the strong de Hass-van Alphen (dHvA) oscillations [8, 26]. Thermoelectric quantum oscillations also verified the topological nodal-line semimetal phase and 3D character of ZrSiS [25].

In general, topological nodal-line semimetals are expected to have high Dirac fermion density owing to Dirac band crossings along a line or loop. The high topological nodal-line fermion density of approximately 10^{20} cm^{-3} has been observed both in ZrSiSe and ZrSiTe through dHvA quantum oscillations [26]. The higher topological nodal-line Fermion density of approximately 10^{23} cm^{-3} arises from the fitting of field-dependent Hall conductivity data with the two-band model [27]. Moreover, perfect electron-hole compensation can induce abnormal MR in the topological semimetal, which can be used in the future magnetic sensors. In this work, we present the detailed analysis of high topological nodal-line fermion density by parabolic MR fitting with a two-band model and semi-classical expression fitting of Hall conductance G_{xy}, which presents the evidence of the topological nodal-line semimetal phase in ZrSiS. Both the Shubnikov-de Hass (SdH) and dHvA oscillations confirm the high-density topological nodal-line fermion in ZiSiS. Perfect electron/hole compensation is also demonstrated by the fitting. Moreover, angular-dependent MR under a magnetic field of 60 T is analyzed, which is the highest magnetic field apply to ZrSiS so far [22, 28].

2 Experiments

ZrSiS single crystals were grown using the chemical vapor transport approach, as described elsewhere [3, 22].

Further details are shown in the Supplemental Material. Hall-bar and four-terminal devices were fabricated to study the electronic/magnetic transport properties. Subsequently, the low-field transport properties were measured using a physical property measurement system (PPMS-9T, Quantum Design). The torque was measured at the High Magnetic Field Laboratory of Chinese Academy of Sciences, China, and high-field measurements were performed in a pulsed magnetic field (up to 60 T) at Wuhan National High Magnetic Field Center, China.

3 Results and discussion

The angular-dependent MR was measured by rotating the sample both in ac and bc planes, as characterized by the angles θ and φ, respectively [inset of Fig. 1(a)]. Clear SdH quantum oscillations were observed in the field-dependent resistivity at various angles in both ac and bc planes, as illustrated in Figs. 1(a) and (b). The resistivity decreases rapidly as the field is tilted from c or b to a axis, indicating high anisotropy in ZrSiS. The magnetic-field-dependent MR shows typical parabola-like features at all the angles. The MR measured under high-pulsed magnetic fields increases with the increase in magnetic field and finally, exhibits nonsaturation up to an intense field of 60 T [Fig. 1(c)]. The maximum resistivity is observed at the angle of approximately 45°. As shown in Fig. 1(d), the angular-dependent resistivity shows an interesting butterfly pattern in both ac and bc planes, indicating significantly anisotropic MR in both ac and bc planes.

We have comprehensively studied the SdH oscillations of ZrSiS in our previous work [22]. For better understanding of quantum oscillations in ZrSiS, dHvA measurements of magnetic torque in ZrSiS at different temperatures and angles were performed, and the results are illustrated in Figs. 2(a) and (b). Two oscillation frequencies can be observed in all the temperatures and angles. Clear quantum oscillations can be observed up to 25 K [Fig. 2(a)], corresponding to the SdH oscillations in our previous work. As evident in Fig. 2(b), both the out-of-plane ($B//c$) and in-plane ($B//ab$) curves exhibit strong dHvA oscillations at low temperatures. Such a feature demonstrates the 3D characteristic of Fermi surface in ZrSiS. There are two dHvA oscillation modes in dHvA quantum oscillations, which can be identified by the frequency of 9 T (low-frequency mode) and that of 244 T (high-frequency mode) after the fast Fourier transform (FFT) processing. The frequency of low-frequency mode obtained in the dHvA study is half of the frequency obtained in the SdH study. However, it corresponds to the dHvA quantum oscillation of 8.4 T in reference [8]. This
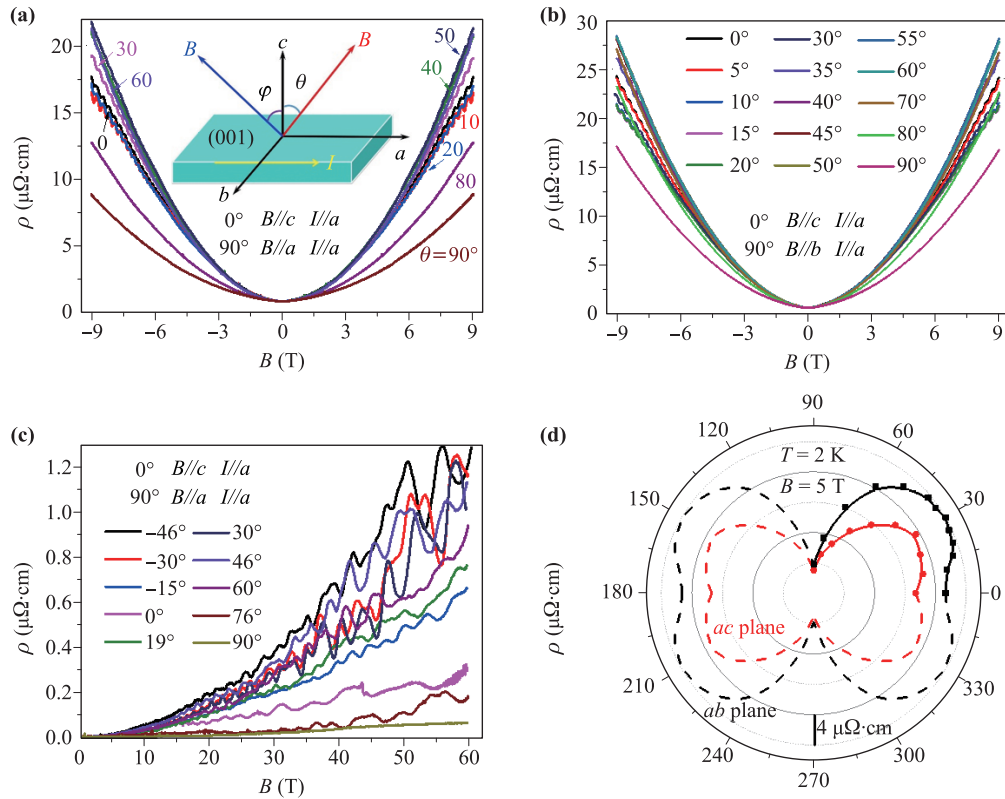
137201-2

Junran Zhang, et al., Front. Phys. 13(1), 137201 (2018)

Fig. 1 **(a, b)** Magnetic-field-dependent resistivity measured at different angles at 2 K in ac and bc planes, respectively. Inset is the schematic structure for angle-dependent magnetotransport measurements in ZrSiS. **(c)** Magnetic-field-dependent resistivity under different θ under a high field (up to 60 T) and 2 K. **(d)** Angular dependence of the resistivity in ac and bc planes, respectively, forming a butterfly shape.

is due to the more sensitive and large Fermi surface in the Torque method or second harmonic. The detailed analysis of dHvA oscillations is shown in Appendix A. The Landau indices (intercept of the fan diagram) are 0.06 and 0.5 for the high-frequency and low-frequency dHvA modes, respectively. The intercept of 0.5 indicates nontrivial transport and demonstrates the Dirac cones. Cyclotron (effective) mass of the electronic states are 0.078 m_e and 0.15 m_e, respectively, by using the Lifshitz–Kosevich formula, as shown in Fig. 2(d). The dHvA oscillations in ZrSiS offer another transport evidence for the 3D nodal-line semimetal phase in ZrSiS.

In order to better understand the nodal-line semimetal phase in ZrSiS, the Dirac Fermion densities and mobilities can be calculated by fitting the magnetic-field-dependent resistivity under all the angles using the two-band model. The longitudinal resistivity in the two-band model is expressed as [29]

$$\rho = \frac{1}{e} \frac{(n_e\mu + n_h\mu') + (n_h\mu + n_e\mu')\mu\mu'H^2}{(n_e\mu + n_h\mu')^2 + [(n_h - n_e)\mu\mu'H]^2}, \quad (1)$$

where n_e (n_h) and μ (μ') represent the Dirac Fermion densities and mobilities of electrons (holes), respec-

tively, and H represents the magnetic field. Parabolic magnetic-field-dependent resistivity can be well fitted by the two-band model both in ac and bc planes, as shown in Figs. 3(a) and (b). The mobilities (Dirac Fermion density) of the electron and hole are 5721 cm^2/(V·s) (6.47×10^{21} cm^{-3}) and 5362 cm^2/(V·s) (6.87×10^{21} cm^{-3}), respectively. The fitting yields n_e/n_h of 0.94, which is consistent with the value of 0.95 obtained by the theoretical calculation (Appendix A). The excellent parabola-like curves of magnetic-field-dependent resistivity in ZrSiS indicate the approximate equality of electron and hole. The perfect electron-hole compensation can induce abnormal MR in ZrSiS and WTe$_2$, which may be applied to the future magnetic sensors [4, 23].

Parabolic curves of magnetic-field-dependent resistivity can be perfectly fitted by the two-band model, resulting in the perfect compensation of electron and hole. In order to confirm this scenario, the Hall conductance G_{xy} is fitted by the semi-classical expression [30]

$$G_{xy} = en_e\mu \frac{\mu B}{(1 + \mu^2 B^2)} + en_h\mu' \frac{\mu' B}{(1 + \mu'^2 B^2)}, \quad (2)$$

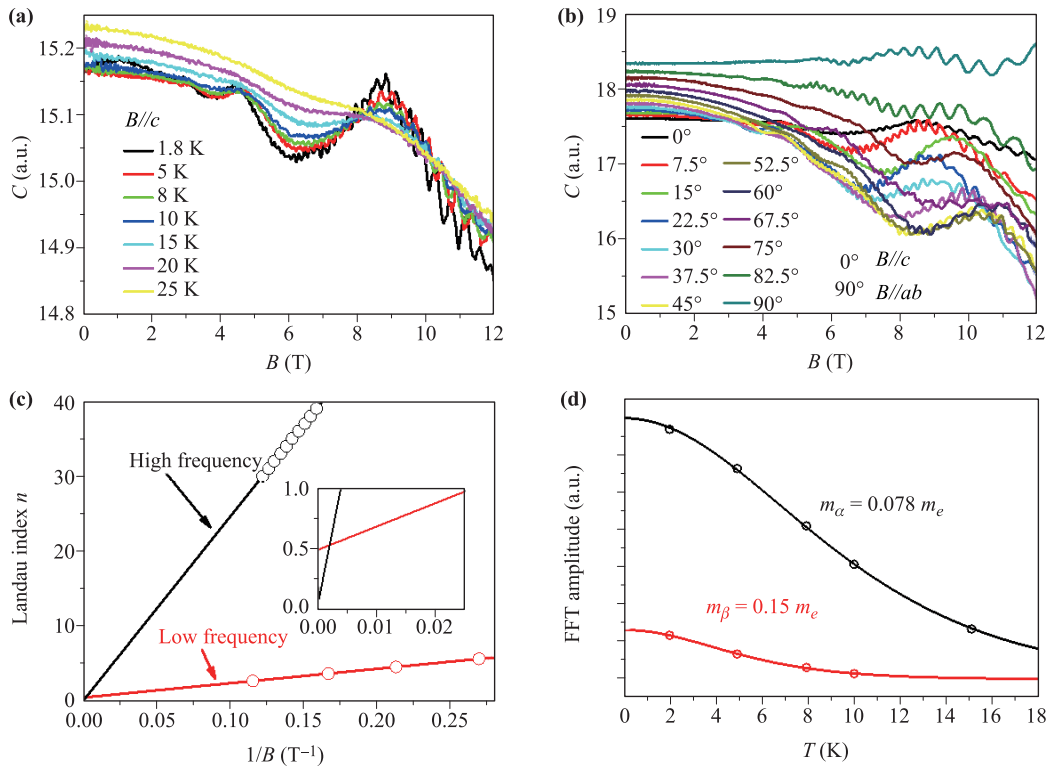where $G_{xy} = \frac{R_{xy}}{R_{xy}^2 + R_{xx}^2}$; R_{xy} is Hall resistance; R_{xx} is

Fig. 2 **(a)** Quantum oscillation measurements of magnetic torque in ZrSiS at different temperatures and **(b)** at different angles at 2 K. **(c)** Landau fan diagrams of the two dHvA oscillation modes. Extrapolated linear fitting provides intercepts, as enlarged near zero in the inset. **(d)** FFT amplitude versus temperature; the solid lines represent the Lifshitz–Kosevich (LK) fitting for the effective mass.
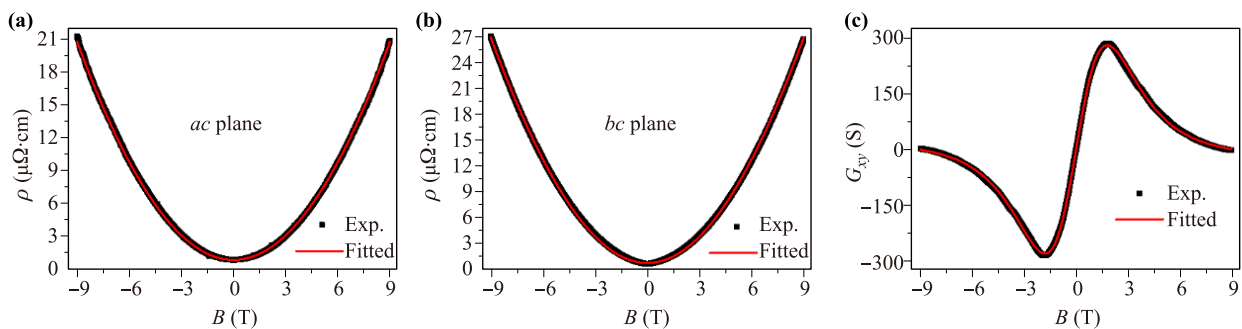

Fig. 3 **(a, b)** Magnetic-field-dependent resistivity fitting with the two-band model in ac and bc planes, respectively. **(c)** Fitting and experimental curves of G_{xy} dependent on the magnetic field at 2 K and $B//c$.

longitudinal resistance; n_e (n_h) and μ (μ') are the Dirac Fermion density and mobility of electrons (holes), respectively. The fitting coincides with the experimental data, as shown in Fig. 3(c). From the fitting, the mobilities (Dirac Fermion density) of electron and hole are 5839 cm^2/(V·s) (6.23×10^{21} cm^{-3}) and 5475 cm^2/(V·s) (6.66×10^{21} cm^{-3}), respectively. This is consistent with the values obtained from the two-band model fitting. The high Dirac fermion densities obtained from the fitting of both the two-band model and semi-classical expression provide a better understanding of Dirac band crossings along a line or loop in ZrSiS.

Both electron (n_e) and hole (n_h) densities are approximately 6×10^{21} cm^{-3}, obtained from the fitting of magnetic-field-dependent resistivity and Hall resistivity via the two-band model and semi-classical expression, respectively, which are larger than those of Dirac semimetal Cd$_3$As$_2$ (1.5×10^{19} cm^{-3}) [6], topological insulator Bi$_2$Se$_3$ (5×10^{18} cm^{-3}) [31], and graphene (5×10^{12} cm^{-3}) [32]. It is known that topological nodal-line semimetals are expected to have a high Dirac fermion density owing to Dirac band crossings along a line or loop. The higher Dirac Fermion density of approximately 10^{23} cm^{-3} from the fitting of field-dependent Hall con-

137201-4

Junran Zhang, et al., Front. Phys. 13(1), 137201 (2018)

ductivity data by the two-band model was reported by Sankar *et al.* [27]. ZrSiSe and ZrSiTe reveal a topological nodal-line semimetal phase owing to the high density of nodal-line fermion (approximately 10^{20} cm^{-3}). The high Dirac Fermion density in ZrSiS observed by our transport measurements verifies the nature of Dirac band crossings along the nodal line. Therefore, the high Dirac fermion density not only provides additional support for the nodal-line state in ZrSiS, but also explains the notable dHvA oscillations in ZrSiS.

Figure 4(a) shows the FFT frequencies of SdH oscillations depending on the angles in the *bc* plane. The low-frequency mode exhibits a weak angular dependence, whereas the high-frequency mode exhibits a clear variation with φ and can be fitted to $F_{2D}/\cos\varphi + F_{3D}$, as illustrated by the solid curve. The relative weight between 3D and 2D components derived from the fitting, F_{3D}/F_{2D}, is approximately 1.8, indicating that the Fermi surface of ZrSiS is of 3D characteristic though a two-dimensional (2D) component also exists. At an angle of approximately 50°, F_β starts to split into two peaks. The 3D characteristic revealed by the fitting FFT-dependent angles is consistent with the analysis of dHvA oscillations.

In order to better understand the Dirac Fermions in ZrSiS, the angle-dependent Berry phase of high-frequency SdH oscillations measured under both a stable magnetic field and high-pulsed magnetic field (up to 60 T) are studied, as shown in Fig. 4. In order to eliminate the uncertainty owing to the Zeeman splitting of oscillation peaks, we filter the waves of high-frequency and low-frequency oscillation modes (Appendix A). In order to obtain a more reliable Berry phase, the LL index of high-frequency F_β is fitted by using a different range of magnetic field. The half-integer and integer LL indices are assigned to the oscillation maximum and minimum, respectively. We obtain intercepts of 0.38 ± 0.04 and 0.55 ± 0.08 when using all the oscillation data between 8–9 T, respectively (Appendix A). When gradually increasing the field range for constructing the fan diagram, all the Berry phases remain trivial although the Berry phase showing small changes, demonstrating the high reliability of the measured Berry phase. Figures 4(b) and (c) show the Berry phase fitting from the high-frequency oscillation at different angles in both *ac* and *bc* planes, respectively. It can be observed that the Berry phases have a slight variation as the angle increases both in *ac* and *bc* planes, but they are still at approximately 0.5, indicating a trivial phase.

The MR under a high-pulsed magnetic field (up to 53 T) was investigated in our previous work [22]. The MR measured at a higher-pulsed magnetic field (up to 60 T)
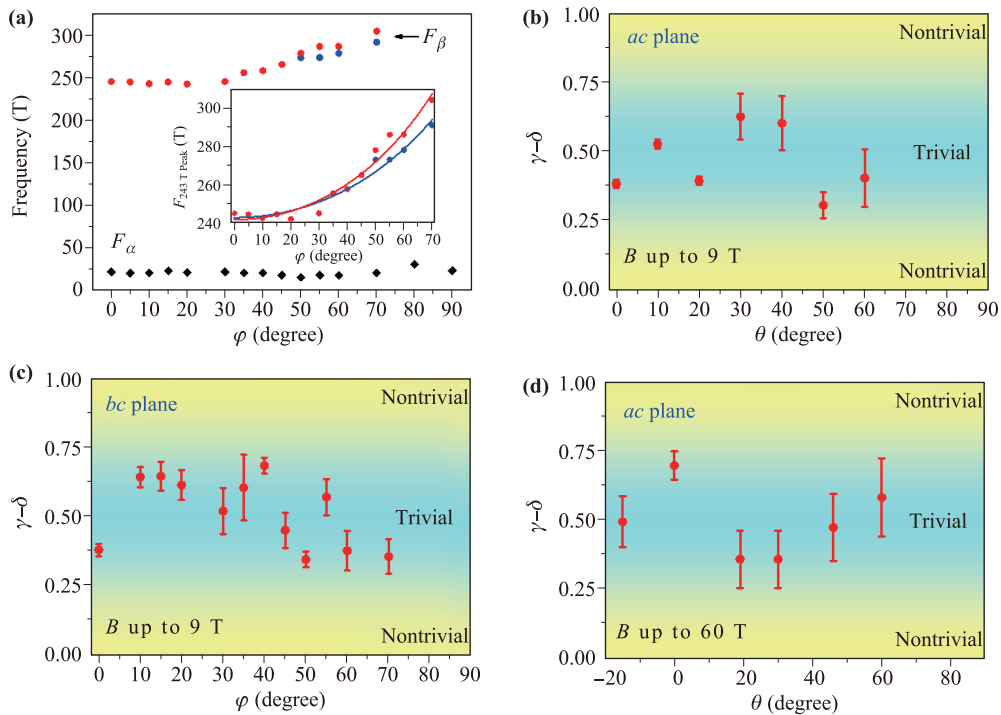

Fig. 4 **(a)** SdH oscillation frequencies dependent on the angles in *bc* plane. Inset is a fitting of the data to $F = F_{3D} + F_{2D}/\cos\theta$ for two splitting peaks of high-frequency oscillation mode. **(b, c)** Berry phase fitting from high-frequency oscillation mode at different θ in *ac* plane and φ in *bc* plane, respectively. **(d)** Berry phase fitting from high-frequency oscillation mode at the different θ with the range of magnetic field from 15 to 30 T.

Junran Zhang, et al., Front. Phys. 13(1), 137201 (2018)

137201-5

is shown in Fig. 1(c). The power factors of MR measured under a high-pulsed field were in the range of 1.44 to 1.8 in the previous work [22], in contrast to the parabolic MR measured under a stable magnetic field. This phenomenon is likely due to the increased number of pockets and stronger anisotropy of the MR response under the higher-pulsed magnetic field. We plot the LL index fan diagram for different θ angles only under 15–30 T, resulting in significant Zeeman splitting of the SdH oscillation peaks under the higher-pulsed magnetic fields [22]. More complex oscillations are induced by the higher-pulsed magnetic fields, as shown in Fig. 4(d). Furthermore, the Berry phase of high frequency shows a similar behavior to that under the stable magnetic field both in the ac and bc planes. Therefore, the Berry phase of the high-frequency mode is insensitive to angle in both the ac and bc planes under stable high-pulsed magnetic fields.

4 Conclusion

In summary, the direct quantum transport evidences of the 3D nodal-line semimetal phase of ZrSiS are observed through angular-dependent resistivity and the combined dHvA and SdH oscillations. The magnetic-field-dependent resistivity curves fitted by a two-band model yield a high nodal-line fermion density of 6×10^{21} cm^{-3} and a perfect electron/hole density ratio of 0.94, coincident with the semi-classical expression fitting of conductance G_{xy} and the theoretical calculations. The dHvA oscillations at all the angles and FFT fitting of SdH provide alternative evidence for the 3D nodal-line semimetal characteristic. Furthermore, we observe that the Berry phase of high-frequency oscillation is insensitive to angles both in the ac and bc planes, which is similar even under a high-pulsed magnetic field (up to 60 T). The comprehensive analyses of quantum behavior in ZrSiS provide a better understanding of the physical nature of topological semimetal, which would determine the potential device applications in the near future.
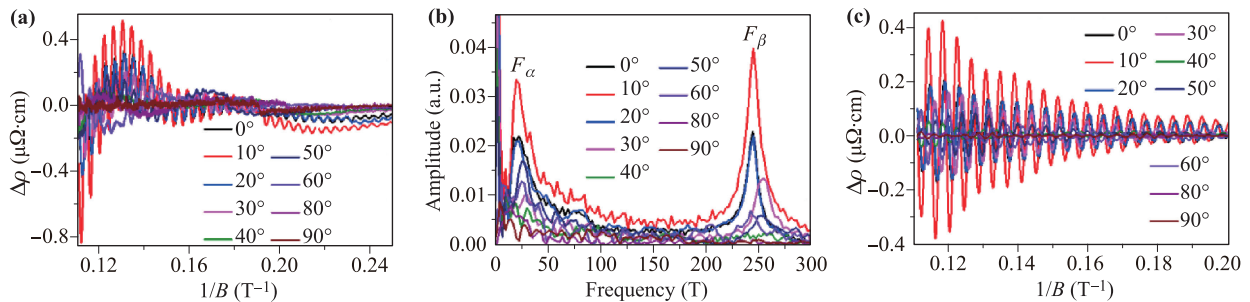
Appendix A Supplemental material

Fig. A1 SdH oscillations of ZrSiS in ac plane. **(a)** SdH oscillation obtained by subtracting background from magnetoresistance measurement, plotted with inverse magnetic field ($1/B$) at different θ angles. **(b)** FFT results of SdH oscillation in (a). **(c)** The high frequency deconvoluted component of SdH oscillation.
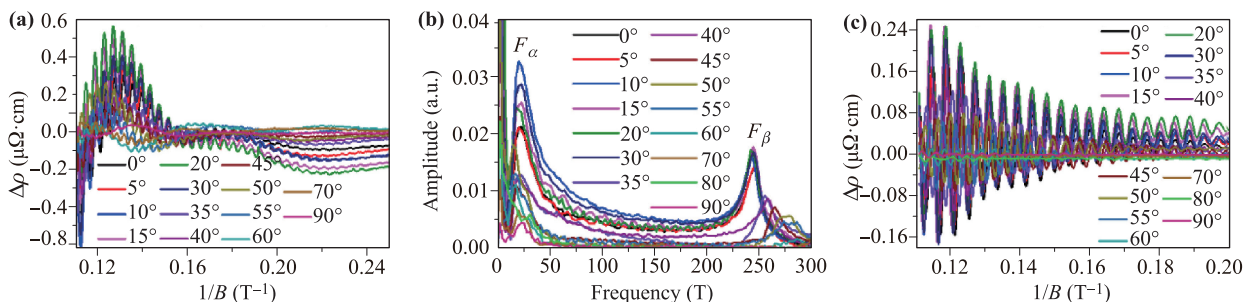

Fig. A2 SdH oscillations of ZrSiS in bc plane. **(a)** SdH oscillation obtained by subtracting background from magnetoresistance measurement, plotted with inverse magnetic field ($1/B$) at different φ angles. **(b)** FFT results of SdH oscillation in (a). **(c)** The high frequency deconvoluted component of SdH oscillation.

137201-6

Junran Zhang, et al., Front. Phys. 13(1), 137201 (2018)

Table A1 Estimated parameters from dHvA oscillations.

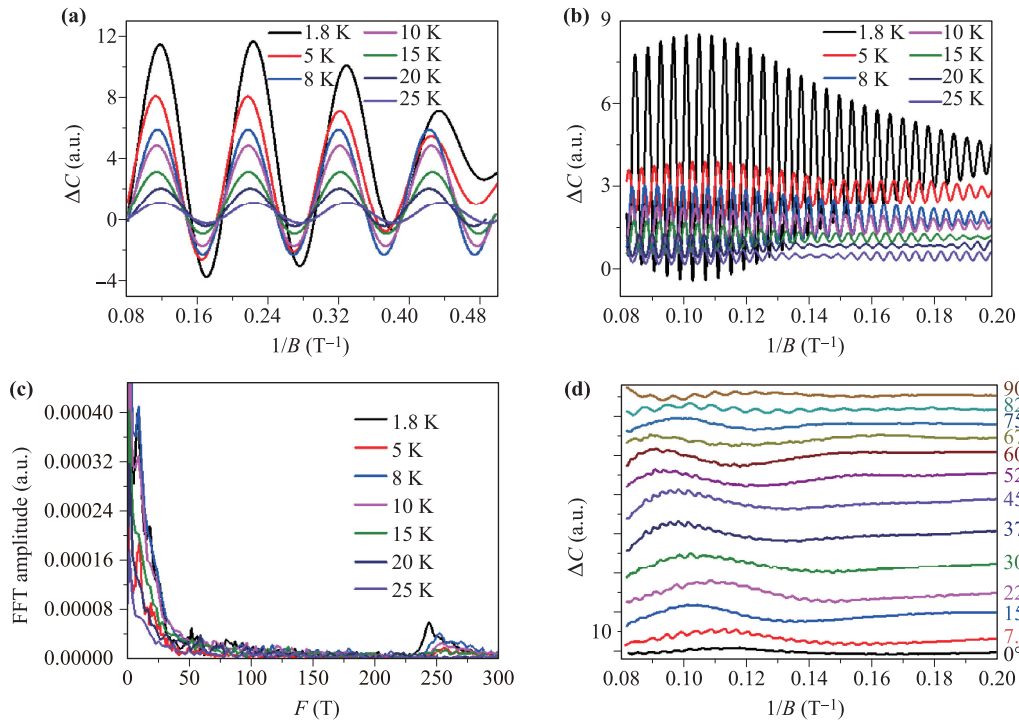| Fermi pockets	F_{SdH} (T)	S_F (10^{-3} Å^{-2})	k_F (Å^{-1})	m_{cyc} (m_e)	v_F (10^5 m·s^{-1})	τ (10^{-13} s)	l (nm)	μ_{SdH} (cm^2·V^{-1}·s^{-1})
α	9	0.86	0.017	0.15	12.77	0.15	19.2	9892
β	244	23.21	0.086	0.1078	6.64	4.52	300.8	5220

Fig. A3 **(a, b)** Low frequency and high frequency oscillations extracted from dHvA oscillations. **(c)** FFT results of dHvA oscillation. **(d)** dHvA oscillations substrated background at different angulars.
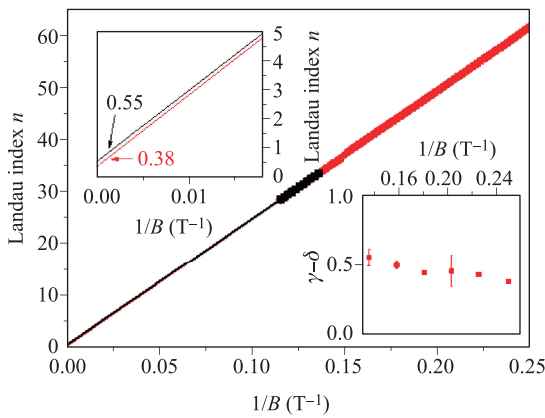

Fig. A4 LL index fan diagram for the high-frequency oscillation mode in ZrSiS under stable magnetic field (up to 9 T). The red line represents linear fit for all LL indices as shown in the left top inset. The black line represents linear fit for LL indices obtained above 8 T. Right bottom inset is the evolution of the intercept with including more low field LL indices into the linear fit.
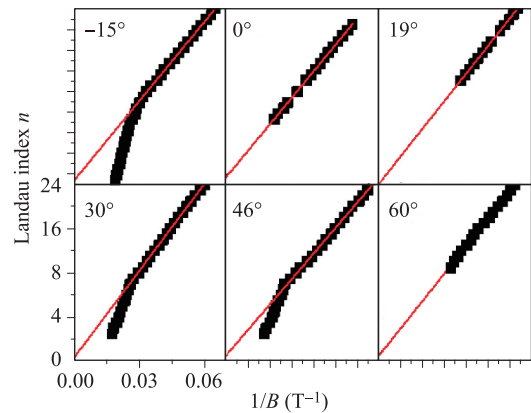
Fig. A5 LL index fan diagram for different θ angles at 15–30 T.

Theoretical calculation

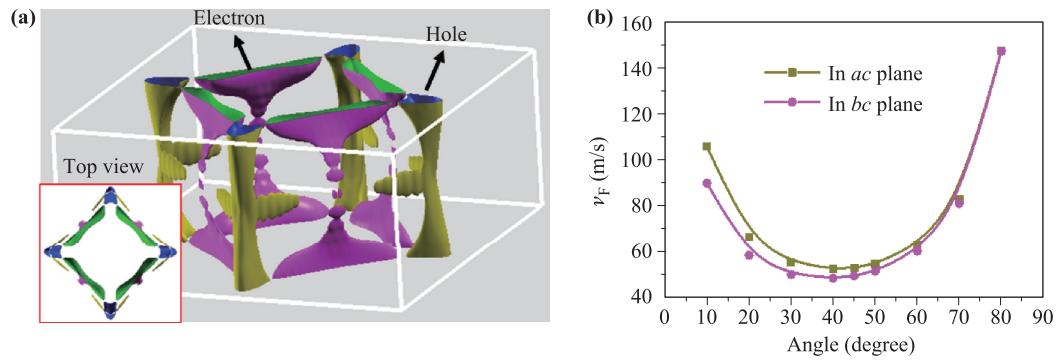The Fermi surface of ZrSiS was drawn to reveal the perfect electron-hole compensation as shown in Fig. A6(a).

Junran Zhang, et al., Front. Phys. 13(1), 137201 (2018)

137201-7

Fig. A6 **(a)** The calculated Fermi surface of ZrSiS. Inset is top view of Fermi surface. **(b)** The calculated Fermi velocity versus angles both in *ac* and *bc* planes.

Inset is the top view of Fermi surface. There are four branches of electron and holes at the Fermi surface, and hole channels show "cylinder-like" morphology. Quantitatively, the calculated ratio between electron and hole concentration is 0.95 that is close to experimental one, which theoretically confirm the perfect electron-hole compensation and result parabolic-like MR perfectly fitted with two-carrier model. The Fermi velocity determines the quality of carrier transport and is related to the MR ratio. We calculated the Fermi velocity against the tilted angles both in *ac* and *bc* planes and the results are shown in Fig. A6(b). We found a systematic evolution of the Fermi velocity versus the angle, where the minimum velocity is near 42° in ac plane and 41° in *bc* plane, respectively. This helps to understand the butterfly shaped MR anisotropy both in *ac* and *bc* planes as shown in Fig. 1(d).

References

1. G. Bian, T. R. Chang, R. Sankar, S. Y. Xu, H. Zheng, T. Neupert, C. K. Chiu, S. M. Huang, G. Chang, I. Belopolski, D. S. Sanchez, M. Neupane, N. Alidoust, C. Liu, B. Wang, C. C. Lee, H. T. Jeng, C. Zhang, Z. Yuan, S. Jia, A. Bansil, F. Chou, H. Lin, and M. Z. Hasan, Topological nodal-line fermions in spin-orbit metal PbTaSe$_2$, *Nat. Commun.* 7, 10556 (2016)

2. Y. Wu, L. L. Wang, E. Mun, D. Johnson, D. Mou, L. Huang, Y. Lee, S. Bud'ko, P. Canfield, and A. Kaminski, Dirac node arcs in PtSn$_4$, *Nat. Phys.* 12(7), 667 (2016)

3. L. M. Schoop, M. N. Ali, C. Strasser, A. Topp, A. Varykhalov, D. Marchenko, V. Duppel, S. S. Parkin, B. V. Lotsch, and C. R. Ast, Dirac cone protected by non-symmorphic symmetry and three-dimensional Dirac line node in ZrSiS, *Nat. Commun.* 7, 11696 (2016)

4. M. N. Ali, J. Xiong, S. Flynn, J. Tao, Q. D. Gibson, L. M. Schoop, T. Liang, N. Haldolaarachchige, M. Hirschberger, N. P. Ong, and R. J. Cava, Large, non-saturating magnetoresistance in WTe$_2$, *Nature* 514, 205 (2014)

5. M. Neupane, S. Y. Xu, R. Sankar, N. Alidoust, G. Bian, C. Liu, I. Belopolski, T. R. Chang, H. T. Jeng, H. Lin, A. Bansil, F. Chou, and M. Z. Hasan, Observation of a three-dimensional topological Dirac semimetal phase in high-mobility Cd$_3$As$_2$, *Nat. Commun.* 5, 3786 (2014)

6. T. Liang, Q. Gibson, M. N. Ali, M. Liu, R. J. Cava, and N. P. Ong, Ultrahigh mobility and giant magnetoresistance in the Dirac semimetal Cd$_3$As$_2$, *Nat. Mater.* 14(3), 280 (2014)

7. C. Shekhar, A. K. Nayak, Y. Sun, M. Schmidt, M. Nicklas, I. Leermakers, U. Zeitler, Y. Skourski, J. Wosnitza, Z. Liu, Y. Chen, W. Schnelle, H. Borrmann, Y. Grin, C. Felser, and B. Yan, Extremely large magnetoresistance and ultrahigh mobility in the topological Weyl semimetal candidate NbP, *Nat. Phys.* 11(8), 645 (2015)

8. J. Hu, Z. Tang, J. Liu, Y. Zhu, J. Wei, and Z. Mao, Evidence of Dirac cones with 3D character probed by dHvA oscillations in nodal-line semimetal ZrSiS, arXiv: 1604.01567 (2016)

9. R. Singha, A. Pariari, B. Satpati, and P. Mandal, Large nonsaturating magnetoresistance and signature of non-degenerate Dirac nodes in ZrSiS, *Proc. Natl. Acad. Sci. USA* 114(10), 2468 (2017)

10. A. Narayanan, M. Watson, S. Blake, N. Bruyant, L. Drigo, Y. Chen, D. Prabhakaran, B. Yan, C. Felser, T. Kong, P. C. Canfield, and A. I. Coldea, Linear magnetoresistance caused by mobility fluctuations in n-doped Cd$_3$As$_2$, *Phys. Rev. Lett.* 114(11), 117201 (2015)

11. H. Li, H. He, H. Z. Lu, H. Zhang, H. Liu, R. Ma, Z. Fan, S. Q. Shen, and J. Wang, Negative magnetoresistance in Dirac semimetal Cd$_3$As$_2$, *Nat. Commun.* 7, 10301 (2016)

12. Z. K. Liu, B. Zhou, Y. Zhang, Z. J. Wang, H. M. Weng, D. Prabhakaran, S. K. Mo, Z. X. Shen, Z. Fang, X. Dai, Z. Hussain, and Y. L. Chen, Discovery of a three-dimensional topological Dirac semimetal Na$_3$Bi, *Science* 343(6173), 864 (2014)

Frontiers of Physics

13. S. Y. Xu, I. Belopolski, N. Alidoust, M. Neupane, G. Bian, C. Zhang, R. Sankar, G. Chang, Z. Yuan, C. C. Lee, S. M. Huang, H. Zheng, J. Ma, D. S. Sanchez, B. Wang, A. Bansil, F. Chou, P. P. Shibayev, H. Lin, S. Jia, and M. Z. Hasan, Topological matter: Discovery of a Weyl fermion semimetal and topological Fermi arcs, *Science* 349(6248), 613 (2015)

14. D. Wu, J. Liao, W. Yi, X. Wang, P. Li, H. Weng, Y. Shi, Y. Li, J. Luo, X. Dai, and Z. Fang, Giant semiclassical magnetoresistance in high mobility $TaAs_2$ semimetal, *Appl. Phys. Lett.* 108(4), 042105 (2016)

15. X. C. Pan, X. Chen, H. Liu, Y. Feng, Z. Wei, Y. Zhou, Z. Chi, L. Pi, F. Yen, F. Song, X. Wan, Z. Yang, B. Wang, G. Wang, and Y. Zhang, Pressure-driven dome-shaped superconductivity and electronic structural evolution in tungsten ditelluride, *Nat. Commun.* 6, 7805 (2015)

16. A. A. Soluyanov, D. Gresch, Z. Wang, Q. Wu, M. Troyer, X. Dai, and B. A. Bernevig, Type-II Weyl semimetals, *Nature* 527(7579), 495 (2015)

17. Y. Zhao, H. Liu, J. Yan, W. An, J. Liu, X. Zhang, H. Wang, Y. Liu, H. Jiang, Q. Li, Y. Wang, X.Z. Li, D. Mandrus, X. C. Xie, M. Pan, and J. Wang, Anisotropic magnetotransport and exotic longitudinal linear magnetoresistance in WTe_2 crystals, *Phys. Rev. B* 92(4), 041104 (2015)

18. M. Neupane, I. Belopolski, M. M. Hosen, D. S. Sanchez, R. Sankar, M. Szlawska, S. Y. Xu, K. Dimitri, N. Dhakal, P. Maldonado, P. M. Oppeneer, D. Kaczorowski, F. Chou, M. Z. Hasan, and T. Durakiewicz, Observation of topological nodal fermion semimetal phase in ZrSiS, *Phys. Rev. B* 93(20), 201104 (2016)

19. M. M. Hosen, K. Dimitri, I. Belopolski, P. Maldonado, R. Sankar, N. Dhakal, G. Dhakal, T. Cole, P. M. Oppeneer, D. Kaczorowski, F. Chou, M. Z. Hasan, T. Durakiewicz, and M. Neupane, Tunability of the topological nodal-line semimetal phase in ZrSiX-type materials (X=S, Se, Te), *Phys. Rev. B* 95(16), 161101 (2017)

20. Q. Xu, Z. Song, S. Nie, H. Weng, Z. Fang, and X. Dai, Two-dimensional oxide topological insulator with iron-pnictide superconductor LiFeAs structure, *Phys. Rev. B* 92(20), 205310 (2015)

21. A. Topp, J. M. Lippmann, A. Varykhalov, V. Duppel, B. V. Lotsch, C. R. Ast, and L. M. Schoop, Nonsymmorphic band degeneracy at the Fermi level in ZrSiTe, *New J. Phys.* 18(12), 125014 (2016)

22. X. Wang, X. Pan, M. Gao, J. Yu, J. Jiang, J. Zhang, H. Zuo, M. Zhang, Z. Wei, W. Niu, Z. Xia, X. Wan, Y. Chen, F. Song, Y. Xu, B. Wang, G. Wang, and R. Zhang, Evidence of both surface and bulk Dirac bands and anisotropic nonsaturating magnetoresistance in ZrSiS, *Advanced Electronic Materials* 2(10), 1600228 (2016)

23. Y. Y. Lv, B. B. Zhang, X. Li, S. H. Yao, Y. Chen, J. Zhou, S. T. Zhang, M. H. Lu, and Y. F. Chen, Extremely large and significantly anisotropic magnetoresistance in ZrSiS single crystals, *Appl. Phys. Lett.* 108(24), 244101 (2016)

24. M. N. Ali, L. M. Schoop, C. Garg, J. M. Lippmann, E. Lara, B. Lotsch, and S. S. Parkin, Butterfly magnetoresistance, quasi-2D Dirac Fermi surface and topological phase transition in ZrSiS, *Sci. Adv.* 2(12), e1601742 (2016)

25. M. Matusiak, J. Cooper, and D. Kaczorowski, Thermoelectric quantum oscillations in ZrSiS, *Nat. Commun.* 8, 15219 (2017)

26. J. Hu, Z. Tang, J. Liu, X. Liu, Y. Zhu, D. Graf, K. Myhro, S. Tran, C. N. Lau, J. Wei, and Z. Mao, Evidence of topological nodal-line fermions in ZrSiSe and ZrSiTe, *Phys. Rev. Lett.* 117(1), 016602 (2016)

27. R. Sankar, G. Peramaiyan, I. P. Muthuselvam, C. J. Butler, K. Dimitri, M. Neupane, G. N. Rao, M. T. Lin, and F. C. Chou, Crystal growth of Dirac semimetal ZrSiS with high magnetoresistance and mobility, *Sci. Rep.* 7, 40603 (2017)

28. S. Pezzini, M. van Delft, L. Schoop, B. Lotsch, A. Carrington, M. Katsnelson, N. Hussey, and S. Wiedmann, Unconventional mass enhancement around the Dirac nodal loop in ZrSiS, arXiv: 1701.09119 (2017)

29. C. Hurd, The Hall effect in Metals and Alloys, Springer Science & Business Media, 2012

30. D. X. Qu, Y. S. Hor, J. Xiong, R. J. Cava, and N. P. Ong, Quantum oscillations and hall anomaly of surface states in the topological insulator Bi_2Te_3, *Science* 329(5993), 821 (2010)

31. K. Eto, Z. Ren, A. Taskin, K. Segawa, and Y. Ando, Angular-dependent oscillations of the magnetoresistance in Bi_2Se_3 due to the three-dimensional bulk Fermi surface, *Phys. Rev. B* 81(19), 195309 (2010)

32. Y. Zhang, Y. W. Tan, H. L. Stormer, and P. Kim, Experimental observation of the quantum Hall effect and Berry's phase in graphene, *Nature* 438(7065), 201 (2005)

Junran Zhang, et al., Front. Phys. 13(1), 137201 (2018)

137201-9

Frontiers of Physics